Sandwich-structured long-wave infrared transparent electromagnetic shielding film using transmittance-enhanced wetting layer/Ag stacked conductive layers

Zhirui Zhang(张智睿), Yuyang Zhang(张雨阳), Le Zhao(赵乐), Zhi Wang(王植), Chi Zhang(张弛), Yao Wu(吴尧), Ruifan Li(李瑞凡), Yonghao Han(韩永昊), and Chaoquan Hu(胡超权)

Citation: Chin. Phys. B, 2026, 35 (**4**): 046803. DOI: 10.1088/1674-1056/ae44f5
http://cpb.iphy.ac.cn; http://iopscience.iop.org/cpb

What follows is a list of articles you may be interested in

Pit density reduction for AlN epilayers grown by molecular beam epitaxy using Al modulation method

Huan Liu(刘欢), Peng-Fei Shao(邵鹏飞), Song-Lin Chen(陈松林), Tao Tao(陶涛), Yu Yan(严羽), Zi-Li Xie(谢自力), Bin Liu(刘斌), Dun-Jun Chen(陈敦军), Hai Lu(陆海), Rong Zhang(张荣), and Ke Wang(王科)

Chin. Phys. B, 2024, 33 (**10**): 106801. DOI: 10.1088/1674-1056/ad7671

Multiphase cooperation for multilevel strain accommodation in a single-crystalline $BiFeO_3$ thin film

Wooseon Choi, Bumsu Park, Jaejin Hwang, Gyeongtak Han, Sang-Hyeok Yang, Hyeon Jun Lee, Sung Su Lee, Ji Young Jo, Albina Y. Borisevich, Hu Young Jeong, Sang Ho Oh, Jaekwang Lee, and Young-Min Kim

Chin. Phys. B, 2024, 33 (**9**): 096805. DOI: 10.1088/1674-1056/ad62e0

Critical behavior in the epitaxial growth of two-dimensional tellurium films on $SrTiO_3$ (001) substrates

Haimin Zhang(张海民), Dezhi Song(宋德志), Fuyang Huang(黄扶旸), Jun Zhang(仉君), and Ye-Ping Jiang(蒋烨平)

Chin. Phys. B, 2023, 32 (**6**): 066802. DOI: 10.1088/1674-1056/acc80d

Coexisting lattice contractions and expansions with decreasing thicknesses of Cu (100) nano-films

Simin An(安思敏), Xingyu Gao(高兴誉), Xian Zhang(张弦), Xin Chen(陈欣), Jiawei Xian(咸家伟), Yu Liu(刘瑜), Bo Sun(孙博), Haifeng Liu(刘海风), and Haifeng Song(宋海峰)

Chin. Phys. B, 2023, 32 (**3**): 036804. DOI: 10.1088/1674-1056/ac76b5

Evolution of microstructure, stress and dislocation of AlN thick film on nanopatterned sapphire substrates by hydride vapor phase epitaxy

Chuang Wang(王闯), Xiao-Dong Gao(高晓冬), Di-Di Li(李迪迪), Jing-Jing Chen(陈晶晶), Jia-Fan Chen(陈家凡), Xiao-Ming Dong(董晓鸣), Xiaodan Wang(王晓丹), Jun Huang(黄俊), Xiong-Hui Zeng(曾雄辉), and Ke Xu(徐科)

Chin. Phys. B, 2023, 32 (**2**): 026802. DOI: 10.1088/1674-1056/ac6865

RAPID COMMUNICATION

Sandwich-structured long-wave infrared transparent electromagnetic shielding film using transmittance-enhanced wetting layer/Ag stacked conductive layers

Zhirui Zhang(张智睿)[1,2,3,†], Yuyang Zhang(张雨阳)[1,2,3,†], Le Zhao(赵乐)[4,†], Zhi Wang(王植)[1,2,3], Chi Zhang(张弛)[1,2,3], Yao Wu(吴尧)[1,2,3], Ruifan Li(李瑞凡)[1,2,3], Yonghao Han(韩永昊)[1,5,‡], and Chaoquan Hu(胡超权)[1,2,3,§]

[1] *State Key Laboratory of High Pressure and Superhard Materials, Jilin University, Changchun* 130012, *China*
[2] *Key Laboratory of Automobile Materials of Ministry of Education, Jilin University, Changchun* 130012, *China*
[3] *School of Materials Science and Engineering, Jilin University, Changchun* 130012, *China*
[4] *National Center for Nanoscience and Technology, Beijing* 100190, *China*
[5] *College of Physics, Jilin University, Changchun* 130012, *China*

(Received 10 November 2025; revised manuscript received 8 January 2026; accepted manuscript online 12 February 2026)

Designing infrared transparent electromagnetic shielding films (ITESFs) is challenging because carrier absorption and carrier transport occur simultaneously. Sandwich structures with Ag inserted into semiconductors can achieve synergy between transparency and electromagnetic shielding effectiveness, but Ag films alone suffer from island growth and optical loss. This work presents a sandwich structure using a transmittance-enhancing conductive layer composed of a wetting layer and Ag (WL/Ag). As a proof of concept, a Bi_2Se_3/Ti WL/Ag/Bi_2Se_3 film was prepared, achieving a long-wavelength infrared transmittance of 77% and a conductivity of 5988 S/cm. The electromagnetic shielding effectiveness reached $\sim$ 22 dB in the X band (8.2–12.4 GHz), meeting the requirement of protecting infrared optoelectronic devices from electromagnetic interference. High-resolution transmission electron microscopy and theoretical calculations showed that the Ti wetting layer enhances performance through high surface energy, low *nk* product values, and admittance matching. We proposed design criteria for wetting layers and identified candidate materials such as Cr. This study provides an optimization strategy for sandwich structures and introduces high-performance ITESFs for infrared optoelectronic devices.

Keywords: transmittance-enhanced, wetting layer/Ag stacked films, sandwich structure, infrared transparent electromagnetic shielding film

PACS: 68.55.–a, 81.15.Cd, 61.30.Hn, 28.41.Qb

DOI: 10.1088/1674-1056/ae44f5 **CSTR:** 32038.14.CPB.ae44f5

1. Introduction

Advanced infrared detection, sensing, and guidance require optical windows with high electromagnetic shielding effectiveness SE ($>$ 20 dB) to suppress electromagnetic interference (EMI). Conventional approaches, such as patterning a metallic mesh, often introduce imaging artifacts and complicate fabrication. Consequently, developing continuous infrared-transparent electromagnetic-shielding films (ITESFs) is urgent.[1–5] For ITESFs thinner than the microwave wavelength, SE typically increases with electrical conductivity σ $\left(\mathrm{SE} = 20\lg\left(1+\frac{377t}{2}\sigma\right)\right)$.[6–9] However, the trade-off between free-carrier absorption and charge transport limits long-wavelength infrared transparency and high conductivity. High-performance ITESFs remain undeveloped.[10–13]

The dielectric-metal-dielectric (DMD) structure, in which metal is inserted between semiconductors, effectively combines transparency and conductivity. Traditional DMDs utilize semiconductors such as ITO, ZnO, WO_3, or WZO and metal conductive layers like Ag or Cu with sub-skin depth thickness.[14–20] However, these semiconductors exhibit limited transparency in the long-wave infrared (LWIR: 8–12 μm) despite high visible-near-infrared transparency. Furthermore, island growth of Ag, bulk absorption and interface reflection result in high losses for both conductivity and transmittance. To suppress Ag island growth, previous studies pre-deposited wetting layers (WLs) such as Cu, Au, or Al.[21–23] Nevertheless, researchers often select WLs based solely on wettability while ignoring the transmission loss caused in specific bands. Consequently, achieving enhanced infrared transparency and high conductivity with traditional DMD structures remains difficult.

In our previous study, Bi_2Se_3 exhibited excellent infrared transparency.[11] However, its low carrier concentration limits its conductivity. In this work, we construct a DMD struc-

[†]These authors contributed equally to this work.
[‡]Corresponding author. E-mail: hanyh@jlu.edu.cn
[§]Corresponding author. E-mail: cqhu@jlu.edu.cn

ture based on the Bi_2Se_3 transparent semiconductor, utilizing a stacked film composed of a Ti WL and Ag (Ti WL/Ag) as the conductive layer. Ultimately, the Bi_2Se_3/Ti WL/Ag/Bi_2Se_3 film achieves an unprecedented integration of high LWIR transmittance (77%) and high conductivity (5988 S/cm). The structure demonstrates an electromagnetic shielding effectiveness of approximately 22 dB in the X band (8.2–12.4 GHz). Combined experiments and theoretical calculations clarify the microscopic mechanism underlying this enhancement of photoelectric properties. Furthermore, we propose design criteria for this new DMD type and identify candidate materials. This study provides a materials optimization strategy for sandwich structures and offers high-performance ITESFs to replace conventional metal grids in infrared detectors.

2. Experiment details

Before deposition, high-purity intrinsic silicon wafers and ZnS substrates (10 mm×10 mm×0.5 mm) were sequentially cleaned using ultrasonication in deionized water, acetone, and anhydrous ethanol for 15 min. The substrates were subsequently dried with nitrogen gas to remove residual surface moisture. Bi_2Se_3, Bi_2Se_3/Ag/Bi_2Se_3, Bi_2Se_3/Ti WL/Ag/Bi_2Se_3 and Bi_2Se_3/Cr WL/Ag/Bi_2Se_3 films were deposited using a multi-target magnetron sputtering system. The base pressure was maintained at 4×10^{-4} Pa, and the working pressure was 0.5 Pa under an Ar flow of 60 sccm. The target-to-substrate distance was 22 cm. All targets were pre-sputtered for 5 min prior to deposition to remove surface oxides. Bi_2Se_3 was sputtered with 60 W RF power, while Ti and Ag were sputtered with 45 W DC power.

Infrared transmission spectra were obtained using a Bruker VERTEX 80v Fourier transform infrared spectrometer. Electrical properties were measured with a Lake Shore 8400 series Hall effect testing system. Film thickness was determined using a Veeco Dektak 150 profilometer. In this study, all thickness of the Bi_2Se_3 layers was uniformly set to 40 nm and determined by the surface profilometer.[24–26] Surface wettability was analyzed with a Kruss DSA30 contact angle instrument. Surface morphology and chemical composition were characterized using a Hitachi SU8010 scanning electron microscope (SEM) equipped with an energy dispersive x-ray spectrometer (EDS). Microstructural analysis was performed using a JEOL JEM-2100F transmission electron microscope (TEM). Electromagnetic shielding effectiveness was measured via a KEYSIGHT PNA-L Network Analyzer (N5234A). Simulation of normalized power loss for various wetting layer materials was conducted using CST Studio software. Volume absorption and interface reflection of the multilayer films were calculated by simulating light field loss within the same software environment.

Based on density functional theory (DFT),[27] first-principles calculations for structural optimization were performed using the DMol3 code.[28] The exchange–correlation effect was treated with the Perdew–Burke–Ernzerhof (PBE) functional within the generalized gradient approximation (GGA).[29] Double numerical plus polarization (DNP) basis sets were used for all atoms.[30] To ensure accuracy, the global orbital cutoff radius in real space was set to 5.3 Å. A vacuum thickness of 23 Å was applied perpendicular to the substrate plane to prevent interaction between adjacent periodic atoms. Brillouin zone integration was sampled using a $6\times6\times1$ Monkhorst–Pack k-point grid. Geometrical structures were fully relaxed until energy, displacement, and force converged to less than 1×10^{-5} Ha, 0.005 Å, and 0.002 Ha/Å, respectively.

3. Results and discussion

To optimize the combined optical and electrical performance, we first systematically investigated the influence of Bi_2Se_3 thickness on LWIR (8–12 μm) transmittance and electrical conductivity. The results show that a Bi_2Se_3 thickness of 40 nm yields the best overall performance, maintaining an LWIR transmittance above 75% with a conductivity of approximately 304 S/cm. Subsequently, an Ag interlayer was introduced to construct a Bi_2Se_3/Ag/Bi_2Se_3 (BAB) sandwich structure, as shown in Figs. 1(a) and 1(b). When the Ag thickness increases from 3 nm to 9 nm, both LWIR transmittance and conductivity exhibit only minor variations. This indicates that Ag does not form a continuous percolated conductive network within this thickness range. In contrast, increasing the Ag thickness to 15 nm significantly enhances conductivity; however, LWIR transmittance decreases markedly because of increased free-carrier absorption and reflection associated with the thicker metallic layer. Therefore, this thickness is unsuitable for applications requiring high infrared transparency. We therefore fixed the Ag thickness at 9 nm and introduced the Ti wetting layer. As shown in Figs. 1(c) and 1(d), a 1 nm Ti layer fails to provide a significant performance change. At 2 nm, the Ti layer significantly increases conductivity with almost no transmittance loss. When the Ti thickness reaches 3 nm, 4 nm, or 5 nm, conductivity improvement is limited, while transmittance is substantially reduced. We also evaluated the thermal radiation transmission efficiency of Bi_2Se_3/Ti (2 nm)/Ag (9 nm)/Bi_2Se_3 (BTAB). As shown in Fig. 1(e), a 7–13 μm camera captured thermal images of a heating platform through a ZnS substrate and a ZnS/BTAB film at different temperatures. The surface temperature of ZnS/BTAB is 65 °C, which is basically consistent with 65.7 °C of the ZnS substrate, indicating that it has a very high LWIR transmittance. Consequently, BTAB achieves optimal LWIR transparent conductive performance, with 77% transmittance and 5988 S/cm conductivity. These results indicate that BTAB possesses high LWIR radiation transmission efficiency with negligible heat loss.

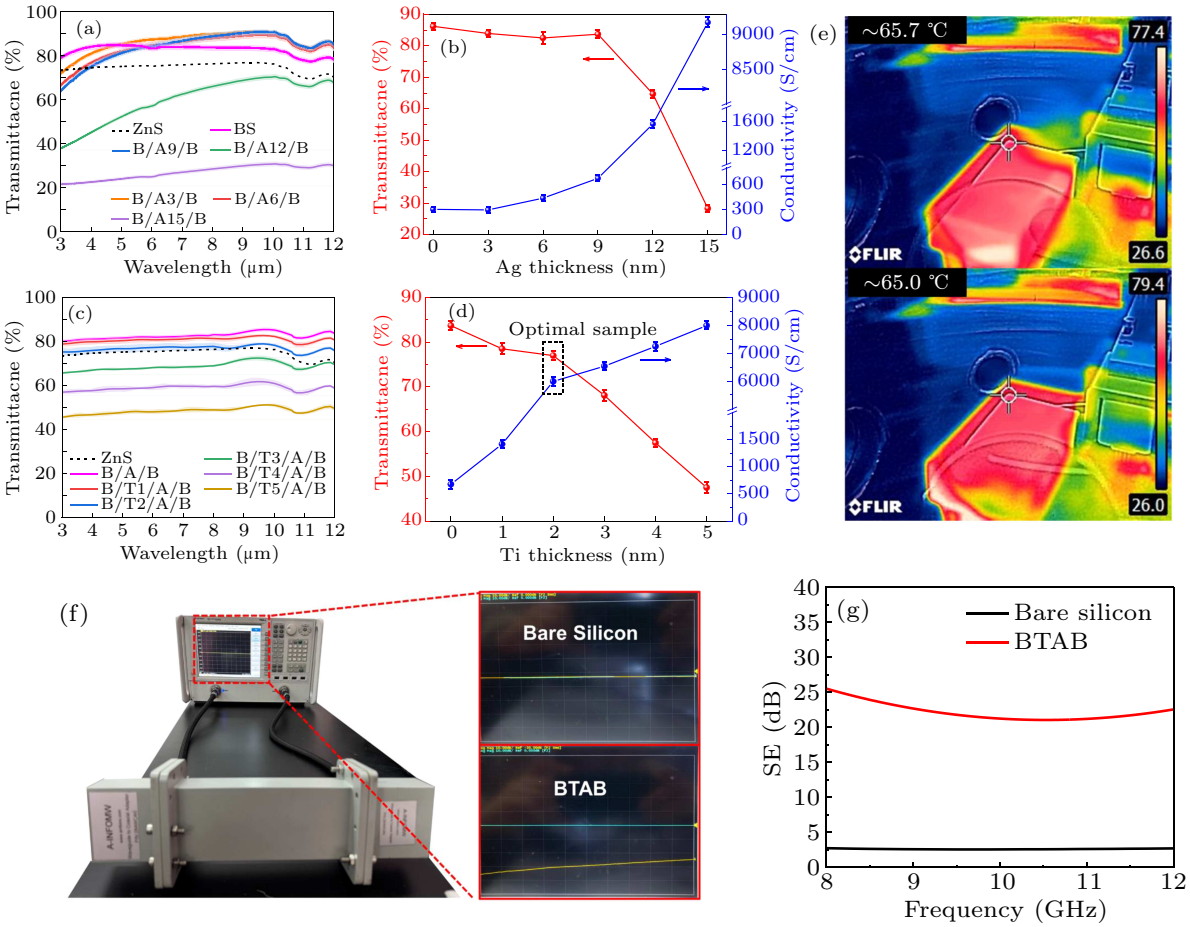

Fig. 1. (a) Mid- to long-wave infrared transmittance (with error band) and (b) conductivity (with error bar) of Bi_2Se_3/Ag/Bi_2Se_3 samples with different Ag layer thicknesses (numbers represent the thickness of the Ag layers, in units of nm). (c) Mid- to long-wave infrared transmittance (with error band) and (d) conductivity (with error bar) of Bi_2Se_3/Ti WL/Ag/Bi_2Se_3 samples with different Ti wetting layer thicknesses (numbers represent the thickness of the Ti layers, in units of nm). (e) Thermal images of the heating platform through ZnS (up) and BTAB/ZnS (down). (f) Self-built electromagnetic shielding effectiveness (SE) test system. (g) The measured (with error band) SE of BTAB.

Finally, to verify the actual electromagnetic shielding performance of BTAB, we measured its electromagnetic shielding effectiveness (SE) in the X band (8.2–12.4 GHz) using a vector network analyzer. As shown in Figs. 1(e) and 1(f), the SE of BTAB is approximately 22 dB, which meets the requirement of protecting infrared optoelectronic devices from electromagnetic interference.[31–34] Additionally, BTAB offers the advantages of a continuous film, overcoming the limitations of conventional metal grids such as poor imaging quality and complex processing.[35] Consequently, BTAB demonstrates significant potential for use as an ITESF.

To investigate the effect of Ti introduction on the structure and conductivity of BAB, we performed experimental characterizations and theoretical calculations. Cohesive energy was determined using first-principles calculations based on density functional theory (DFT). Surface morphology was observed via scanning electron microscopy (SEM), and the contact angle was characterized to assess wettability. As shown in Figs. 2(a)–2(d), 69 nm Ag films exhibit typical island growth without a Ti wetting layer. This morphology indicates poor wettability of Ag on pure Bi_2Se_3 and a preference for three-dimensional island formation. As the thickness increases to 1215 nm, the Ag surface gradually smoothens as islands merge to form a continuous film. In contrast, introducing a Ti wetting layer achieves a continuous and uniform surface morphology at an Ag thickness of only 9 nm. This result demonstrates that Ti promotes two-dimensional layer-by-layer growth of the Ag film. AFM images shown in Figs. 2(e)–2(h) also demonstrate that in the presence of Ti WL, the surface root roughness of Ag films decreases gradually from 4.01 nm to 0.72 nm, indicating that the introduction of Ti WL is more conducive to the layered growth of Ag films.

To further verify the enhancement of wettability by Ti, we conducted contact angle tests on samples of Ag (9 nm)/Bi_2Se_3, Ag (9 nm)/Ti (1 nm)/Bi_2Se_3, Ag (9 nm)/Ti (2 nm)/Bi_2Se_3, and Ag (9 nm)/Ti (4 nm)/Bi_2Se_3. The results show that the contact angle increases from 85.9° (without Ti) to 93.6° (with 4 nm Ti). This change indicates that the Ti interlayer reconstructs the interfacial energy of the system. The balance between the solid–vapor interfacial energy (γ_{sv}) and the solid–liquid interfacial energy (γ_{sl}) has shifted, resulting in an increase in the surface diffusion length of Ag adatoms, enabling them to migrate more freely to find low-energy lattice sites rather than being pinned at the initial nucleation sites. This enhanced mo-

bility is crucial for suppressing 3D island coalescence and fostering the development of a continuous, layered Ag film at a lower thickness.

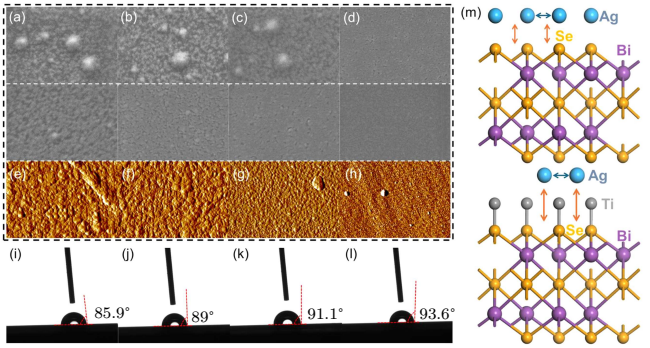

Fig. 2. (a)–(d) SEM images of Ag thicknesses of 6 nm, 9 nm, 12 nm and 15 nm without (up) and with (down) Ti wetting layer. (e)–(h) AFM images of Ag thicknesses of 6 nm, 9 nm, 12 nm and 15 nm with Ti wetting layer. (i)–(l) Contact angle images for Ag thicknesses of 6 nm, 9 nm, 12 nm and 15 nm in the presence of Ti wetting layers. (m) DFT calculation model of cohesive energy for Ag (up) and Ti WL/Ag (down) on Bi_2Se_3 surface.

In combination with SEM surface morphology analysis, the insertion of Ti effectively alters the interfacial energy. This alteration is closely related to the transformation of Ag film growth from three-dimensional island formation to continuous layer-by-layer growth. Furthermore, DFT calculations elucidate the differential growth mechanisms from an energy perspective. As shown in Fig. 2(m), the cohesive energy of Ag on Ti is approximately −0.49 eV/atom, which is energetically more favourable compared to +0.46 eV/atom on Bi_2Se_3. This provides a physical explanation for the suppression of island growth and the transition to a continuous layer-by-layer growth mode. These findings support the conclusion that Ti reduces the diffusion energy barrier for Ag adatoms. Consequently, Ag atoms undergo planar diffusion and migration, yielding a more continuous and smoother film.

Cross-sectional high-resolution transmission electron microscopy (HRTEM) in Figs. 3(a)–3(c) reveals that the Ag film grown on the Bi_2Se_3/Ti WL surface exhibits high two-dimensional continuity and crystal orientation matching. As shown in Figs. 3(b) and 3(c), the lattice fringes of the Bi_2Se_3 thin film are clearly discernible. The measured interplanar spacings are 3.18 Å and 2.11 Å, corresponding to the (015) and (110) crystal planes of the standard Bi_2Se_3 reference (JCPDS No. 33-0214). These results indicate high crystal quality and the expected structural phase. Furthermore, continuous and distinct lattice fringes near the Bi_2Se_3/Ti WL interface provide microscopic evidence that the Ti WL promotes the transition of Ag growth from an island-like to a continuous layer-by-layer mode. A smooth and structurally continuous interface reduces interfacial scattering and contact resistance, facilitating the formation of an efficient conductive channel. Consequently, the wetting effect of Ti reduces the percolation threshold thickness of the Ag film, resulting in a flat surface and enhanced conductive paths that significantly increase conductivity.[36] When the Ti WL is too thin (1 nm), it provides insufficient wettability, causing Ag to grow in island mode with low conductivity. Conversely, excessive Ti WL thickness (35 nm) leads to significant bulk absorption, substantially reducing overall transmittance.[37–40]

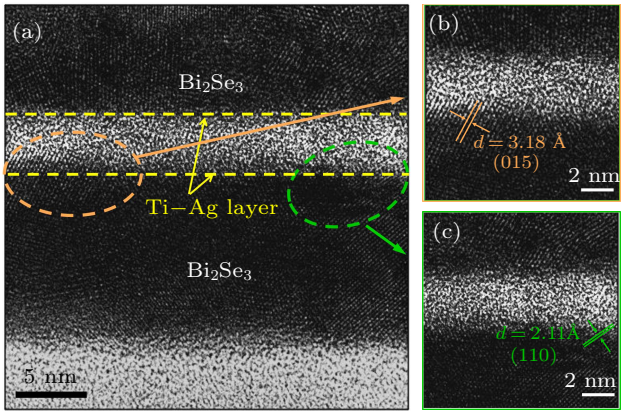

Fig. 3. (a) Cross-sectional HRTEM images of BTAB. (b)–(c) Zoom-in images of the selected areas with corresponding colors in (a).

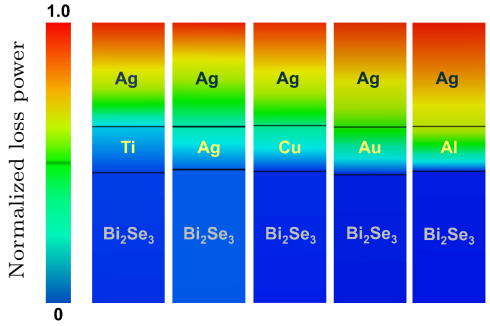

Fig. 4. Light field loss images of WL/Ag obtained by CST simulation, red indicates high loss, blue indicates low loss.

To study the effect of Ti on the transparency of the BAB structure, we simulated the bulk absorption and interface reflection of the multilayer films with and without a metal WL. Light field loss was simulated using CST Studio software. The results indicate that Ti absorbs significantly less LWIR light than Ag or traditional WL metals, such as Cu, Au, and Al, at equivalent thicknesses. The transparency of Ti is comparable to the Bi_2Se_3 substrate, which exhibits high LWIR transparency. According to

$$A = 4\pi nk \int_0^d |E(z)|^2 \mathrm{d}z / |E_0|^2 \lambda, \tag{1}$$

the lower absorption of Ti can be attributed to its comparatively lower nk product value,[41,42] with $nk_{\mathrm{Ti}} = 80.8$, $nk_{\mathrm{Ag}} = 754.5$, $nk_{\mathrm{Cu}} = 527.3$, $nk_{\mathrm{Au}} = 988.5$, and $nk_{\mathrm{Al}} = 1846.4$. The approximate reflectivity ($\widetilde{R}$) of the entire multilayer film can be calculated from

$$\widetilde{R} = \left| r_0 + \sum_{s=1}^{4} r_s \, \mathrm{e}^{-\mathrm{i}2(\delta_1+\delta_2+\cdots+\delta_s)} \right|^2. \tag{2}$$

When only Ag is present, interface reflectivity is 7.7%. When the WL is Cu, Al, or Au, reflectivity values are 5.9%, 10.3%,

and 17.1%, respectively. Notably, reflectivity is only 1.4% when the WL is Ti. Compared to other metals, Ti effectively weakens interface reflectivity. This effect is attributable to the minimal difference between $r_2 + r_3$ and $r_0 + r_1 + r_4$ (approximately 2.2%), indicating that Ti achieves admittance matching with Ag and Bi_2Se_3.[5]

To customize ITESFs for diverse application scenarios, we identified candidate materials for the wetting layer. High surface energy originates from the high density of unpaired d-orbital electrons in the metal surface layer.[40,41] Consequently, we screened transition metals with unpaired d-electrons from the fourth to sixth periods (groups IIIB-VIII). Metals with higher surface energy than Ti, such as Cr, Fe, Ni, and Nb, were selected as candidate WLs, as shown in Figs. 5(a) and 5(b).[42]

We calculated the *nk* product values of these candidate WL materials for Bi_2Se_3-based DMD structures to evaluate the performance of different WL/Ag combinations. The results are shown in Fig. 5(c). Ti, Cr, Fe, Ni, W, and Os all satisfy the criteria of $nk < 500$ and reflectivity $< 10\%$. To validate this theoretical prediction, we fabricated BCAB samples using Cr as the wetting layer and performed a comparative analysis with BTAB and BAB samples. The results are presented in Fig. 5(d) and the inset. The LWIR transparent conductive properties of the BCAB sample ($T_{\mathrm{LWIR}} \approx 86\%$, $\sigma \approx 2380$ S/cm, FoM $\approx 1.67 \times 10^{-3}$) are comparable to those of the optimal BTAB sample ($T_{\mathrm{LWIR}} \approx 77\%$, $\sigma \approx 5988$ S/cm, FoM $\approx 1.74 \times 10^{-3}$). The higher transmittance of BCAB compared to BTAB aligns with our theoretical prediction of low reflection (admittance matching), despite slightly lower conductivity. Nevertheless, the conductivity of BCAB is significantly higher than that of the BAB sample without a wetting layer ($T_{\mathrm{LWIR}} \approx 84\%$, $\sigma \approx 679$ S/cm, FoM $\approx 1.54 \times 10^{-3}$). This observation is consistent with the theoretical expectation that Cr, with its high surface energy, promotes Ag layer-by-layer growth. Overall, these results confirm the accuracy of our theoretical predictions and material screening criteria.

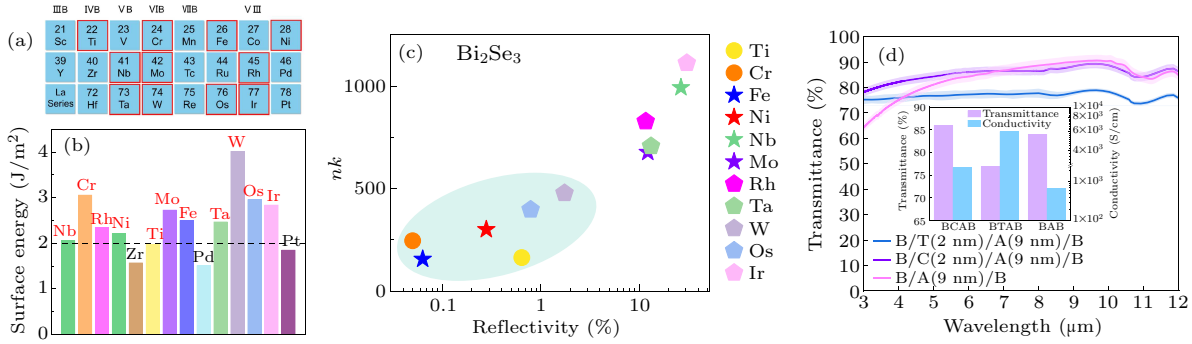

Fig. 5. Elemental composition of candidate WL materials and (b) surface energy. (c) *nk* product values of candidate WL materials and reflection of Bi_2Se_3-based DMDs. (d) Mid- to long-wave infrared transmittance (3–12 μm, with error band) of BCAB, BTAB and BAB samples. The illustration shows a comparison of the transmittance and conductivity properties of BCAB, BTAB and BAB samples.

4. Summary

In summary, the introduction of a Ti WL/Ag stacked layer into Bi_2Se_3 achieves a sandwich-structured film with optimal LWIR transparent conductive performance ($T_{\mathrm{LWIR}} \approx 77\%$, $\sigma \approx 5988$ S/cm) and an electromagnetic shielding effectiveness of 22 dB in the X band. This enhanced performance results from the high surface energy of Ti, which promotes the layer-by-layer growth of Ag and increases conductivity. Additionally, the low *nk* product of Ti and its admittance matching with the multilayer structure reduce bulk absorption and interface reflection, thereby improving transparency. Based on these findings, we identified candidate conductive layer materials, including Cr, Fe, Ni, W and Os WL/Ag. These continuous ITESFs are expected to replace conventional metal grids, addressing the limitations of poor imaging quality and complex fabrication processes.

Acknowledgements

This work was supported by the Natural Science Foundation of Beijing, China (Grant No. 4222086) and the National Natural Science Foundation of China (Grant Nos. 52032004 and 52272153).

References

[1] Maiti R, Patil C, Saadi M A S R, Xie T, Azadani J G, Uluutku B, Amin R, Briggs A F, Miscuglio M, Van Thourhout D, Solares S D, Low T, Agarwal R, Bank S R and Sorger V J 2020 *Nat. Photon.* **14** 578
[2] García de Arquer F P, Talapin D V, Klimov V I, Arakawa Y, Bayer M and Sargent E H 2021 *Science* **373** eaaz8541
[3] Chen X, Li H, Chen W, Mei Z, Azarov A, Kuznetsov A and Du X 2024 *Chin. Phys. Lett.* **41** 037305
[4] Lu B, Liu R, Li S, Lu R, Chen L, Ye Z and Lu J 2020 *Chin. Phys. Lett.* **37** 098501
[5] Khurgin J, Bykov A Yu and Zayats A V 2024 *eLight* **4** 15
[6] Lecocq H, Garois N, Lhost O, Girard P F, Cassagnau P and Serghei A 2020 *Compos. Part B Eng.* **189** 107866
[7] Gupta T K, Singh B P, Teotia S, Katyal V, Dhakate S R and Mathur R B 2013 *J. Polym. Res.* **20** 169
[8] Nasouri K, Shoushtari A M and Mojtahedi M R M 2016 *J. Polym. Res.* **23** 71

[9] Al-Saleh M H and Sundararaj U 2009 *Carbon* **47** 1738
[10] Cui C, Ding Q, Yu S, Yu C, Jiang D, Hu C, Gu Z and Zhu J 2023 *Prog. Mater. Sci.* **136** 101112
[11] Hu C, Zhou Z, Zhang X, Guo K, Cui C, Li Y, Gu Z, Zhang W, Shen L and Zhu J 2023 *Light Sci. Appl.* **12** 98
[12] Mohammadi M, Xie R, Hadaeghi N, Radetinac A, Arzumanov A, Komissinskiy P, Zhang H and Alff L 2023 *Adv. Mater.* **35** 2206605
[13] Zhang L, Zhou Y, Guo L, Zhao W, Barnes A, Zhang H T, Eaton C, Zheng Y, Brahlek M, Haneef H F, Podraza N J, Moses H W Chan, Gopalan V, Rabe K M and Engel-Herbert R 2016 *Nat. Mater.* **15** 204
[14] Cai L, Zhou J, Hu H, Xu X, Jiang Z H and Hong W 2023 *IEEE Trans. Antennas Propag.* **71** 9101
[15] Yin Y, Gao T, Xu Q, Cao G, Chen Q, Zhu H, Lan C and Li C 2020 *J. Mater. Chem. A* **8** 10973
[16] Liu Z, Zou Y, Ji C, Chen X, Hou G, Zhang C, Wan X, Guo L J, Zhao Y and Zhang X 2021 *ACS Appl. Mater. Interfaces* **13** 58539
[17] Choi J, Bang G, Lee T, Tran V T B, Bae J S and Choi D 2022 *Nano Lett.* **22** 3133
[18] Wang H, Tang C, Shi Q, Wei M, Su Y, Lin S and Dai M 2021 *Ceramics International* **47** 7666
[19] Al-Kuhaili M F 2023 *Solar Energy* **250** 209
[20] Li H, Shen H, Zhang J, Li Y, Du Z, Bai H, Chen J, Zheng J, Yue Z and Zeng J 2023 *Ceramics International* **49** 36225
[21] Jamnig A, Pliatsikas N, Abadias G and Sarakinos K 2021 *Appl. Surf. Sci.* **538** 148056
[22] Martinez-Cercos C, Paulillo B, Maniyara R A, Rezikyan A, Bhattacharyya I, Mazumder P and Pruneri V 2021 *ACS Appl. Mater. Interfaces* **13** 46990
[23] Jeong E, Ikoma Y, Lee T, Kim H, Yu S M, Lee S G, Bae J S, Han S Z, Lee G H, Choi D, Choi E A and Yun J 2022 *Acta Materialia* **223** 117484
[24] Malpure N N, Patil S R, Sali J V, Pugliese D, Afre R A and Khadayate R S 2025 *Photonics* **12** 1219
[25] Qaid S M H, Ghaithan H M, Al-Asbahi B A and Aldwayyan A S 2022 *Coatings* **12** 549
[26] Karim I, Rokon S M N, Naeem M A H, Robin I K, Ahmed A N, Sattar Md A and Sabur Md A 2025 *Omega* **10** 49490
[27] Parr R G and Yang W 1995 *Annual Review of Physical Chemistry* **46** 701
[28] Delley B 2000 *J. Chem. Phys.* **113** 7756
[29] Perdew J P 1996 *Phys. Rev. Lett.* **77** 3865
[30] Delley B 1990 *J. Chem. Phys.* **92** 508
[31] Liao D, Zheng Y, Ma X and Fu Y 2023 *Opt. Express* **31** 32200
[32] Sharma K, Kaur H and Bahel S 2023 *J. Electroceram.* **51** 71
[33] Manobalan S, Suryasarathi B and Sumangala T P 2024 *Polym. Compos.* **45** 15804
[34] Cheng C, Liu Y, Ma R and Fan R 2022 *Compos. Part A Appl. Sci. Manuf.* **155** 106842
[35] Wang S J, Qin W T, Guan T Y, Liu J Y, Cai Q N, Zhang S, Zhou Le, Zhang Y, Wu Y Z and Tao Z S 2024 *eLight* **4** 11
[36] Li S, Zhang X, Zhang P, Sun X, Zheng H and Zhang W 2018 *Nanoscale Res. Lett.* **13** 259
[37] Guan M, Wang L, Zhang Y, Wang D, Wang Q and Liu J 2023 *Mater. Today Commun.* **37** 107540
[38] Li D, Pan Y, Liu H, Zhang Y, Zheng Z and Zhang F 2022 *Nanomaterials* **12** 3540
[39] Sedghi M, Zabolian H and Khashei H 2023 *Thin Solid Films* **770** 139760
[40] Liao J, Chen N, Xu S, Qian R, Luo G, Hu S and Zhu W 2024 *Thin Solid Films* **788** 140
[41] Ciesielski A, Skowronski L, Trzcinski M, Górecka E, Trautman P and Szoplik T 2018 *Surf. Sci.* **674** 73
[42] Mash I D and Motulevich G P 1973 *Sov. Phys. JETP* **36** 516